New interatomic potentials of W, Re and W-Re alloy for radiation defects

Yangchun Chen [a, b], Yu-Hao Li [c], Ning Gao [d, *], Hong-Bo Zhou [c], Wangyu Hu [b], Guang-Hong Lu [c], Fei Gao [b, e], Huiqiu Deng [a, b, **]

[a] Department of Applied Physics, School of Physics and Electronics, Hunan University, Changsha 410082, China
[b] College of Materials Science and Engineering, Hunan University, Changsha 410082, China
[c] Department of Physics, Beihang University, Beijing 100191, China
[d] Laboratory of Advanced Nuclear Material, Institute of Modern Physics, Chinese Academy of Sciences, Lanzhou 730000, China
[e] Department of Nuclear Engineering and Radiological Sciences, University of Michigan, Michigan 48109, USA

HIGHLIGHTS

- New interatomic potentials for W, Re and W-Re based on the F-S formalism have been developed.
- The W potential predicts the relative stability of interstitial dislocation loops in W bulk as reported in experiments.
- For Re-Re interaction, the basic properties of Re bulk are good in agreement with the experimental results.
- For W-Re interaction, the key point-defect properties of Re in W are well reproduced.
- These potentials are applicable for describing the evolution of irradiation defects in W and W-Re alloys.

ARTICLE INFO

ABSTRACT

Tungsten (W) and W-based alloys have been considered as promising candidates for plasma-facing materials (PFMs) in future fusion reactors. The formation of rhenium (Re)-rich clusters and intermetallic phases due to high energy neutron irradiation and transmutations significantly induces the hardening and embrittlement of W. In order to better understand these phenomena, in the present work, new interatomic potentials of W-W, Re-Re and W-Re, suitable for description of radiation defects in such alloys, have been developed. The fitted potentials not only reproduce the results of the formation energy, binding energy and migration energy of various radiation defects and the physical properties from the extended database obtained from DFT calculations, but also predict well the relative stability of different interstitial dislocation loops in W, as reported in experiments. These potentials are applicable for describing the evolution of defects in W and W-Re alloys, thus providing a possibility for the detailed understanding of the precipitation mechanism of Re in W under irradiation.

© 2018 Elsevier B.V. All rights reserved.

1. Introduction

Nuclear fusion energy is a promising future energy source. Developing the suitable radiation-resistant materials is one of the key technological challenges to safely apply such fusion energy in future. Tungsten and W-based alloys have been considered as possible candidates for the first wall PFMs in future magnetic confinement nuclear fusion energy devices [1—4], because of its high melting point, high thermal conductivity and low sputtering yield [5,6]. However, the neutrons generated in fusion reactions will result in the generation of several transmutation elements from W, such as rhenium (Re), osmium (Os), tantalum (Ta) and hafnium (Hf), through the transmutation reactions [7,8]. Among these elements, Re is a main product, whose concentration may reach to several percent after five years of fusion operation [7,8]. Even though the solubility of Re in W is high (close to 30 at.% [9,10]), the radiation-induced precipitation can be observed when the Re concentration is much less than its saturation solid solubility

[11–17]. Experimental observations [11–15] indicate that Re precipitates in W have different phases from pure W crystals, forming the σ phase (WRe) or χ phase (WRe$_3$). More recently, the ion beam irradiation experiments of W-2Re alloys by Xu et al. at 300 °C and 500 °C also clearly confirmed the Re-rich clusters in bulk W [16,17]. These clusters and precipitates may significantly increase the hardening and embrittlement of W, and then seriously reduce the lifetime of reactors [12–15]. Therefore, it is very critical and necessary to understand the formation mechanism of Re clusters and precipitates in W.

Based on density functional theory (DFT) calculations, the interactions between the solute atoms (e.g. Re and Os) and radiation-induced defects (e.g. self-interstitial atom (SIA) and vacancy) in bulk W have been studied [18–27], which provide the possible formation mechanisms of Re-rich clusters in W under irradiation. Especially, the binding energy of Re solute pairs in bulk W is confirmed to be quite weak [18,19], while the strong attractive interactions between Re and point defects have been found [20–27]. Recent work based on an energy model by the cluster expansion (CE) formalism has also revealed a direct relationship between excess vacancy concentrations and the formation of Re solute-rich clusters in W-Re system [27]. It should be noted that this CE approach does not take into account SIA defects as well as mixed W-Re and Re-Re dumbbells during the cluster formation. While several studies have suggested that the interstitial-mediated mechanism would also be responsible for the clustering of Re atoms in bulk W [20–22]. Such a mechanism consists of a series of mixed dumbbell (e.g. W-Re dumbbell) rotations and transitions so that the mixed nature of a dumbbell is preserved and solutes can be transported over long distances without the formation of vacancies. Furthermore, this mechanism extends the one-dimensional SIA diffusion into three-dimensional mixed-dumbbell transport process with activation energies even lower than that of vacancy diffusion. It should be noted that because of the computational limitation, the above studies focus only on the small clusters or static processes. Thus, the kinetics and related formation mechanisms of large Re-rich clusters and sub-soluble intermetallic phases in irradiated W and W-Re still remain unclear.

To solve the above questions, the classical or accelerated molecular dynamics (MD) simulations are generally used with reliable empirical potentials. It should be noted that there is only one report about the cross interatomic potentials for W-Re binary system, which is the embedded-atom method (EAM) interatomic potential developed recently by Bonny et al. [28]. This potential provides an excellent tool to study the plasticity in W-Re alloys at atomic level, but the key point-defect properties, as well as Re atom/cluster under irradiation, in bcc W still need improvement. For example, the attractive interactions between Re and a vacancy is clearly lower than the DFT value and the relative energy difference between the mixed W-Re <111> and <110> dumbbells is also overestimated. The interactions between Re atom/cluster and point defects play an important role in the Re precipitation and the evolution of Re-defects in irradiated W [20–22,25–27], and therefore, a new W-Re potential suitable for radiation defect properties should be developed in order to explore more precisely the Re precipitation mechanisms in radiated W bulk.

For W-W interaction, more than 30 interatomic potentials have been developed (see Ref. [29] for a review). Very recently, Ehemann et al. [30] developed a modified embedded-atom method (MEAM) potential for W at high pressure and Szlachta et al. [31] developed a potential for W within the Gaussian approximation potential (GAP) framework. Among these potentials, Finnis-Sinclair (F-S) and EAM forms are attractive due to their high computational efficiency, especially for the simulations of high-energy collision cascades with millions of atoms in the system. The most common W

potential used is the Ackland-Thetford potential (AT-potential) [32], which was developed from the original FS-potential (developed by Finnis and Sinclair) [33] and recently modified by Juslin and Wirth (JW-potential) [34]. However, the formation energy of SIA predicted by this potential is lower than the DFT result; and the energy differences between different dumbbells are also distinct from the DFT predictions. Derlet et al. developed another F-S type potential (DN-potential) [35], which reproduces well the correct energies of various SIA configurations in tungsten. However, it predicts the negative thermal expansion at the temperature above 300 K (as shown in the following section "Results and discussion"), which is in conflict with the experimental results [36]. In addition, three potentials were developed by Marinica et al. (MV2-, MV3- and MV4-potentials) [37] to model the radiation defects and dislocations in W; however, these potentials are still required to improve the SIA formation energies and surface energies so that they are able to well reproduce the DFT results. In 2014, a potential was developed by Wang et al. (WZ-potential) [38] by focusing on self-interstitial defects and the thermal expansion of W, but it could not correctly predicts the relative stability of radiation-induced dislocation loops. In order to simulate radiation damages, the relative stability of radiation-induced dislocation loops (e.g., with the Burgers vectors of 1/2<111> or <100>) in W should also be reproduced. Recent experimental observations have revealed that the 1/2<111> loops instead of the <100> ones are the dominated SIA-cluster defects, especially at low temperatures [39–41]. DFT calculations of loop formation energy also show that a 1/2<111> loop is the lower energy state than a <100> loop with the same number of SIAs [42]. Thus, considering the important role of dislocation loop in understanding radiation damage in W, the relative stabilities of different loops are also required for a suitable W potential used in understanding its radiation damages.

For Re-Re interaction, a few empirical potentials have been developed in the literature. Baskes et al. [43] proposed a modified EAM (MEAM) model for 18 hcp metals, including Re element. They studied the properties of vacancy, di-vacancy, surface and stacking fault, and the results indicate that except the di-vacancy, the other properties are well in agreement with experimental results; however, this model includes the terms of angular forces, which seriously limit the computational efficiency for large scale simulations. Hu et al. [44] also proposed another modified EAM form (MAEAM) for hcp Re. Although this potential reproduces well the experimental lattice constants, cohesive energy, vacancy formation energy and five independent elastic constants, the expression is too complicated because it includes the energy modification term. The recent Re potential developed by Bonny et al. [28] overestimates the formation energy of vacancy (as compared to DFT value) and the melt point (by about 40%).

To study the radiation damage properties of W-Re system, new interatomic potentials based on F-S formalism for W-W, Re-Re, and W-Re have been developed in the present work by fitting to the extended database from experiments as well as the first-principles DFT calculations. These potentials are then expected to be suitable for describing the evolution of defects in W and W-Re alloy.

2. Methodology

2.1. Potential formalism and energy model

In the present work, the interactions for a W-Re system are described based on the original F-S formalism [33], that is, the total energy E_t can be expressed as

$$E_t = E_p + E_N. \tag{1}$$

E_p is a pair-potential summation and calculated by

$$E_p = \frac{1}{2} \sum_{ij} V(r_{ij}), \tag{2}$$

where r_{ij} is the distance between atom i and j. E_N is the N-body (or many-body) term and can be written as

$$E_N = \sum_i F(\rho_i), \tag{3}$$

with

$$F(\rho_i) = -A\sqrt{\rho_i}, \tag{4}$$

and

$$\rho_i = \sum_j \phi(r_{ij}). \tag{5}$$

ρ_i is the local electronic charge density at site i which is constructed by a superposition of atomic charge density ϕ.

Thus, the F-S potentials for W-Re system include eight functions (F_W, F_{Re}, V_{WW}, V_{ReRe}, ϕ_{WW}, ϕ_{ReRe}, ϕ_{WRe} and V_{WRe}), where the first six ones can be determined by using the properties of pure W and Re components, and the last two cross functions should be fitted to the properties of W-Re alloys. For pure elements, the parameter A in equation (4) is set to 1, and the functions V_{WW}, V_{ReRe}, ϕ_{WW} and ϕ_{ReRe} are defined as cubic splines

$$V(r) = \sum_{k=1}^{N_k} a_k (r_k - r)^3 H(r_k - r), \tag{6}$$

$$\phi(r) = \sum_{k=1}^{N_k} A_k (R_k - r)^3 H(R_k - r), \tag{7}$$

where $H(x)$ is the Heaviside step function, r_k and R_k denote the positions of cubic spline knots, a_k and A_k are the knots coefficients, respectively.

In addition, the invariant transformations have been taken into considered during the fitting processes. For pure species, the potential functions are subject to the transformations $\widehat{T_1}$ and $\widehat{T_2}$ [33,45,46].

$$\widehat{T_1} = \begin{cases} \varnothing(r) \to S\varnothing(r) \\ F(\rho) \to F(\rho/S) \end{cases}, \tag{8}$$

$$\widehat{T_2} = \begin{cases} F(\rho) \to F(\rho) + C\rho \\ V(r) \to V(r) - 2C\varnothing(r) \end{cases}, \tag{9}$$

where C and S are arbitrary constants, but ensure that $\rho_0 = 1$ and $F' = 0$ at the equilibrium lattice state. These transformations do not affect any properties of the pure elements but gives an equal contribution to the local electron density of each elements as building the W-Re cross potential.

For W-Re cross potential (or alloy potential), the pair-potential function V_{WRe} is chosen by combining linearly the existed elemental pair-interaction functions $V_{WW}(r)$ and $V_{ReRe}(r)$ as in the case of our previous work [47–49]:

$$V_{WRe}(r) = \frac{1}{2}\left[u_a V_{WW}\left(r\frac{r_a}{r_c}\right) + u_b V_{ReRe}\left(r\frac{r_b}{r_c}\right) \right], \tag{10}$$

$$r_c = \frac{1}{2}[r_1(W) + r_1(Re)], \tag{11}$$

where u_a, u_b, r_a and r_b are the fitted parameters, $r_1(W)$ and $r_1(Re)$ represent the first-neighbor distance in elements W and Re, respectively. The cross function ϕ_{WRe} between W and Re atoms is represented by

$$\phi_{WRe}(r) = \sum_{k=1}^{N_k} B_k (R_k - r)^3 H(R_k - r), \tag{12}$$

with the knots coefficients B_k.

For use in collision cascades' simulations, the pair interaction functions are then connected smoothly to the Bizersack-Zeigler universal function [50] at short-range distance by using the Fermi function as in the case of our previous paper [51].

2.2. Fitting strategy

The parameters in the potential functions were fitted by minimizing the weighted mean-squared deviation of the selected properties from their target values (the existed experimental results and/or DFT calculation ones) through the simulated annealing method [52] and conjugate gradient algorithm [53]. The objective function U is expressed as following:

$$U = \sum \omega_i [f_i(\lambda) - F_i]^2, \tag{13}$$

where ω_i is weighted coefficient, f_i and F_i are the calculated properties and the reference values, respectively. The value f_i depends on the fitting potential parameters λ. The smaller the value of U, the closer $f_i(\lambda)$ is to the reference value F_i. The weight ω_i of each data item i in the fit determines how well the final fit will reproduce each property.

For elements W and Re, the target material properties fitted here are cohesive energy, lattice constant, vacancy formation and elastic constants. As for W, the SIA defect formation energies are also included. Since an empirical universal relationship (or Rose equation) developed by Rose et al. [54] can well reproduce the dependence of energy on volume for a broad range of materials, it is also fitted in the present work to ensure the reasonable dependence of the interatomic interactions on equilibrium spacing.

For the W-Re alloy, we focus on the behaviors of Re atoms and clusters and their interactions with point defects in bcc W. Here, the following properties are mainly included in the fitting: the formation energy of a single substitutional Re atom, the formation energies of one Re interstitial atom in various configurations (e.g. the mixed dumbbell) and the binding energies of one solute Re atom with some typical point defects, such as one vacancy and one SIA.

The dynamics fitting approach is employed [51], and the simulation box is set to $10a_0 \times 10a_0 \times 10a_0$ (a_0 is the lattice constant) with N ($N = 2000$) atoms, adding or deleting atoms as needed to get the defect configurations. The formation energy of a vacancy is defined as

$$E_v^f = E_{(N-1)W} - (N-1)E_C^W, \tag{14}$$

where $E_{(N-1)W}$ is the energy of the supercell with (N-1) W atoms, E_C^W is the cohesive energy of W. The formation energy of a SIA is

Table 1
Fitted parameters for W-W, Re-Re, and W-Re potentials. R_k and r_k denote the positions of cubic spline knots (Å). A_k, a_k and B_k are knots coefficients (eV/Å^3). The other parameters are dimensionless.

	W	Re
A_1 (R_1)	$0.157394320944321 \times 10^0$ (5.3)	$0.985237382995892 \times 10^0$ (4.9)
A_2 (R_2)	$0.256286340126315 \times 10^0$ (4.9)	$-0.199947692011378 \times 10^1$ (4.5)
A_3 (R_3)	$0.113652618869651 \times 10^1$ (4.5)	$0.508531638694275 \times 10^1$ (4.1)
A_4 (R_4)	$0.121424681568044 \times 10^1$ (4.1)	$-0.181599856411676 \times 10^1$ (3.8)
A_5 (R_5)	$-0.596325448809099 \times 10^1$ (3.7)	$-0.386903822888978 \times 10^1$ (3.5)
A_6 (R_6)	$0.132583861458088 \times 10^1$ (3.3)	$-0.117208437037924 \times 10^1$ (3.2)
A_7 (R_7)	$0.102158201513837 \times 10^2$ (3.0)	$0.708185679838769 \times 10^0$ (2.9)
A_8 (R_8)	$0.132127443316801 \times 10^3$ (2.7)	$0.185272925240220 \times 10^3$ (2.7)
A_9 (R_9)	$-0.136815683673490 \times 10^2$ (2.5)	$-0.275576871657117 \times 10^3$ (2.5)
A_{10} (R_{10})	$-0.158146510950533 \times 10^3$ (2.4)	$0.226219972548473 \times 10^3$ (2.4)
a_1 (r_1)	$0.335024387589958 \times 10^{-1}$ (5.3)	$0.595770379726787 \times 10^{-1}$ (5.4)
a_2 (r_2)	$0.163033349357780 \times 10^{-1}$ (5.0)	$-0.484711987882270 \times 10^{-1}$ (5.1)
a_3 (r_3)	$0.200272930919956 \times 10^{-1}$ (4.8)	$-0.109652213718314 \times 10^0$ (4.8)
a_4 (r_4)	$0.442544764151892 \times 10^{-1}$ (4.6)	$-0.410315510883489 \times 10^{-2}$ (4.6)
a_5 (r_5)	$-0.360458890109753 \times 10^{-1}$ (4.4)	$-0.138574583022008 \times 10^0$ (4.4)
a_6 (r_6)	$-0.782637369706724 \times 10^0$ (4.2)	$0.413428944917866 \times 10^0$ (4.2)
a_7 (r_7)	$0.198354466486430 \times 10^0$ (4.0)	$0.340306548603778 \times 10^0$ (4.0)
a_8 (r_8)	$0.339548790839008 \times 10^0$ (3.8)	$-0.250510224189427 \times 10^0$ (3.8)
a_9 (r_9)	$0.115329264087981 \times 10^1$ (3.6)	$-0.540850305859432 \times 10^0$ (3.6)
a_{10} (r_{10})	$0.209267214785968 \times 10^1$ (3.4)	$-0.135653498299661 \times 10^0$ (3.4)
a_{11} (r_{11})	$-0.433898470837892 \times 10^1$ (3.2)	$0.446211760956630 \times 10^0$ (3.2)
a_{12} (r_{12})	$0.226278158796390 \times 10^1$ (3.0)	$0.442194641630830 \times 10^1$ (3.0)
a_{13} (r_{13})	$0.486982659394188 \times 10^1$ (2.8)	$-0.154393092265007 \times 10^1$ (2.8)
a_{14} (r_{14})	$0.117595527893821 \times 10^2$ (2.7)	$0.237130024717419 \times 10^2$ (2.7)
a_{15} (r_{15})	$0.426754828593335 \times 10^2$ (2.6)	$-0.125654971505844 \times 10^2$ (2.6)
a_{16} (r_{16})	$-0.150658274191899 \times 10^3$ (2.5)	$-0.165857183335557 \times 10^2$ (2.5)
a_{17} (r_{17})	$0.128062389467005 \times 10^3$ (2.4)	$0.180581396801872 \times 10^2$ (2.4)
S	$0.8928098176946668 \times 10^{-2}$	$0.1032547624567184 \times 10^{-1}$
C	$0.4724430700345457 \times 10^{-1}$	$0.5080717529461719 \times 10^{-1}$

	W-Re
B_1 (R_1)	$0.143200269341469 \times 10^{-1}$ (4.9)
B_2 (R_2)	$0.993456092144462 \times 10^{-2}$ (4.0)
B_3 (R_3)	$-0.702829467907214 \times 10^{-1}$ (3.1)
B_4 (R_4)	$0.413991996187913 \times 10^1$ (2.5)
u_a	$0.202711025088156 \times 10^1$
u_b	$0.394652353081478 \times 10^1$
r_a	$0.274215842608393 \times 10^1$
r_b	$0.407372241629925 \times 10^1$
r_c	$0.274050000000000 \times 10^1$

defined as

$$E^f_{SIA} = E_{(N+1)W} - (N+1)E^W_C, \tag{15}$$

and the formation energy of a substitutional Re atom is calculated by

$$E^f_{sub-Re} = E_{(N-1)W+Re} - (N-1)E^W_C - E^{Re}_C, \tag{16}$$

where $E_{(N-1)W+Re}$ is the total energy of the supercell with $(N-1)$ W atoms and a substitutional Re atom; E^W_C and E^{Re}_C are the cohesive energies of W and Re elements.

The formation energy of an interstitial Re atom (formed Re-W mixed dumbbell) is expressed as

$$E^f_{Re-W} = E_{(N-1)W+Re-W} - NE^W_C - E^{Re}_C, \tag{17}$$

and the formation energy of two Re atoms (formed Re-Re dumbbell) is expressed as

$$E^f_{Re-Re} = E_{(N-1)W+Re-Re} - (N-1)E^W_C - 2E^{Re}_C, \tag{18}$$

where $E_{(N-1)W+Re-W}$ and $E_{(N-1)W+Re-Re}$ are the total energies of a W-Re system with $N-1$ W atoms and a Re-W or Re-Re dumbbell, respectively.

The binding energy between a Re atom and a vacancy is calculated by

$$E^b_{Re-Vac} = E^f_{sub-Re} + E^f_{Vac} - E^f_{Re-Vac}, \tag{19}$$

and the binding energy between a substitutional Re atom and a SIA is calculated by

$$E^b_{Re-W} = E^f_{sub-Re} + min\left(E^f_{SIA}\right) - E^f_{Re-W}, \tag{20}$$

and the binding energy between a substitutional Re atom and an interstitial Re atom is calculated by

$$E^b_{Re-Re} = E^f_{sub-Re} + min\left(E^f_{Re-W}\right) - E^f_{Re-Re}, \tag{21}$$

where $min\left(E^f_{SIA}\right)$ and $min\left(E^f_{Re-W}\right)$ are the formation energies of the most stable SIA and a Re-solute interstitial atom, respectively. It should be noted that in above equations, the positive values of the binding energy indicate the attraction between two defects.

After the fitting procedure and optimization, all the potential parameters for W-Re system are listed in Table 1 and the dependences of potential function on atomic distance or electronic density are then shown in Fig. 1.
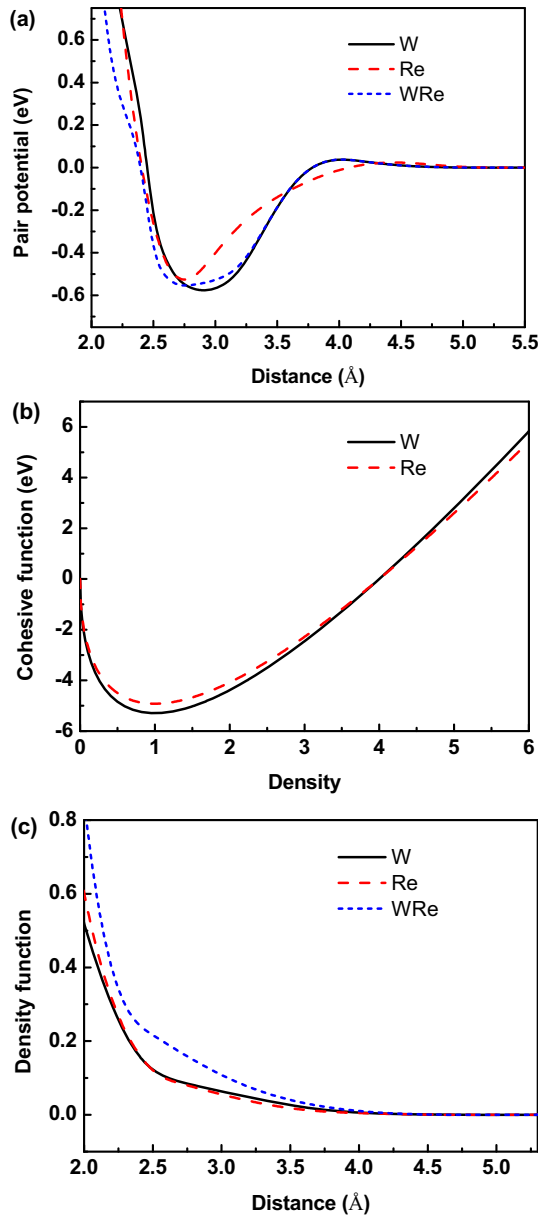
Fig. 1. Dependence of the potential function on atomic distance or electronic density: (a) pair potential, (b) cohesive function and (c) density function.

3. Results and discussion

3.1. Validation of the present W potential

In order to evaluate the reliability of the fitted potentials, the basic properties of bulk W, including lattice constant, elastic constants, cohesive energy, bulk modulus, structural energy differences, vacancy and interstitial formation energies, vacancy migration energy and surface energy, are calculated and listed in Table 2. Here, the properties marked with a symbol "*" are those considered in the fitting processes. The corresponding experimental values, DFT calculations data and predictions of other interatomic potentials (FS [33], AT [32], JW [34], DN [35], WZ [38], MV2 [37]) are also presented for comparison.

From Table 2, we can see that almost all the empirical potentials possess the same lattice constant as the experimental result [55], except that the MV2 potential gives a slightly lower value. The

cohesive energy calculated by all the potentials is equal to the experimental measurement [55]. Furthermore, the fitted body-centered cubic (bcc) lattice is confirmed as the most stable structure, comparing to other structures including the simple cubic (sc), face-centered cubic (fcc), hexagonal close-packed (hcp) and diamond, although there is some discrepancy for the structural energy difference between the potentials' calculations and DFT results [56,57]. As for elastic constants, the results of all the potentials agree well with those from the experiments [58]. Vacancy formation energies in W from all potentials closely agree with the DFT results [59] and within the range of experimental data [60]. The migration energy of a single vacancy in W calculated with the present potential is 1.91 eV, slightly higher than the DFT (1.78 eV) [59] and experimental values (1.78 ± 0.1 eV) [60]; while the FS, AT and JW potentials (1.44 eV) underestimate and DN potential (2.07 eV) overestimates this property. The diffusion activation energy of a single vacancy predicted by our potential is in good agreement with the experiment data [60]. It is also clear that the formation energy of a <111> SIA (9.46 eV) and the energy difference between the <110> and <111> SIAs (0.34 eV) calculated with the present potential, DN and WZ potentials are in good agreement with the DFT results [59]; however, FS and AT potentials underestimate the formation energy of SIA dumbbells, and MV2 potential overestimates it. JW potential gives a suitable value for the formation energy of a <111> dumbbell for W atoms, but overestimates the energy difference between the <111> and <110> dumbbells. The surface energies of several low index orientations are also listed in Table 2. It can be found that all the potentials indicate the (110) surface to be the most stable one, which is the same as the DFT result [29]. From the above comparison, we can see that the basic properties of bcc W can be well described by this new fitted potential.

For validating the properties at high temperatures, the thermal expansion has also been calculated by the present potential. The present results, together with the experiments [36] and predictions by other empirical potentials (AT, DN, MV2), are shown in Fig. 2 for the temperatures between 293 and 3500 K. For comparison, the starting reference temperature for MD simulations is set to 293 K, which is the same as the experimental condition [36]. The MD simulations of 2000 atoms under NPT ensemble at zero-pressure yield a thermal-expansion curve. Each MD simulation runs for 300,000 steps with a 1fs time step, and the thermal expansion for each temperature is determined by averaging over 100,000 simulation steps after full relaxations. As shown in Fig. 2, the thermal expansion from the AT potential is higher than that of the experimental results while the predication of DN presents a negative thermal expansion, which is in conflict with the experimental results [36]. The results from the present potentials closely follow the experimental data [36], suggesting that the potential is reliable over a broad temperature range. Furthermore, the melting temperature was determined using the present potential by following the solid-liquid coexistence method [61] with MD simulations. In this work, a $20a_0 \times 20a_0 \times 20a_0$ simulation box containing 40,000 W atoms was built. The melting temperature determined with this method is 4580 ± 10 K for W, which is about 900 K higher than the experimental value of 3695 K [62]. Based on DN and AT potentials, the melting points are approximately 3750 K and 5200 K, respectively, calculated by Fikar et al. [63]. The melting point using the WZ potential is 4100 K [38].

Fig. 3 shows the dependence of pressure on the relative volume V/V_0 calculated with four potentials (AT, DN, MV2 and the present potential), where V_0 is the zero-pressure volume obtained from the NPT MD simulations at 0 K. The results have been compared with the data from shock experiments [64]. It is clear from Fig. 3 that the results predicted by the present potential agree quite well with

Table 2

Calculated physical properties of W using the present potential, in comparison with the experimental values and calculations of DFT or other empirical potentials. Properties indicated by "*" were included in the potential fit. The following values are listed: the lattice parameter a (Å), the cohesive energy E_c (eV), the bulk modulus B and elastic constants C_{11}, C_{12}, C_{44} (GPa), the vacancy formation energy E_v^f (eV), vacancy migration energy E_v^m (eV) and vacancy diffusion activation energy Q_v (eV), the formation energy of the divacancy E_{2v}^f (eV), the binding energy of the divacancy E_{2v}^b (eV), the SIA defect formation energy E_i^f (eV), the surface energy E_{Surf} (J/m^2), the structural energy difference ΔE (eV) and the melting point (K).

Property	Present	Exp.	DFT	FS [33]	AT [32]	JW [34]	DN [35]	WZ [38]	MV2 [37]
a^*	3.1652	3.1652[a]	3.172[d]	3.1652	3.1652	3.1652	3.1652	3.1652	3.1400
E_c^*	8.9	8.9[a]	8.48[d]	8.9	8.9	8.9	8.9	8.9	8.9
B	310	310[b]	305[e]	310	310	310	310	309	320
C_{11}^*	522	522[b]	526[e]	522	522	522	525	520	544
C_{12}^*	204	204[b]	194[e]	204	204	204	203	204	208
C_{44}^*	161	161[b]	146[e]	161	161	161	159	161	160
E_v^{f*}	3.54	3.67[c]	3.56[f]	3.63	3.63	3.63	3.56	3.58	3.49
E_v^m	1.91	1.78[c]	1.78[f]	1.44	1.44	1.44	2.07	1.43	1.85
Q_v	5.45	5.45[c]	5.34[f]	5.07	5.07	5.07	5.63	5.01	5.34
E_{2v1nn}^f	6.67		6.71[g]	6.83	6.83	6.83	6.55	6.71	6.48
E_{2v2nn}^f	6.70		6.93[g]	6.86	6.86	6.86	6.74	6.75	6.59
E_{2v1nn}^b	0.41		0.41[g]	0.43	0.43	0.43	0.51	0.45	0.50
E_{2v2nn}^b	0.38		0.19[g]	0.40	0.40	0.40	0.38	0.41	0.39
$E_{i<111>}^{f*}$	9.46		9.55[f]	7.81	8.92	9.50	9.55	9.58	10.52
$E_{i<110>}^{f*}$	9.80		9.84[f]	8.45	9.64	10.16	9.84	9.86	10.82
$E_{i<100>}^{f*}$	11.01		11.49[f]	8.66	9.82	10.30	11.51	11.53	12.86
$E_i^f Tra$	10.30		11.05[f]	8.82	9.97	10.47	11.00	10.93	11.94
$E_i^f Oct$	10.71		11.68[f]	8.87	9.98	10.41	11.71	11.72	12.64
$E_{surf}\{110\}$	2.541		3.197[h]	2.575	2.575	2.575	2.402	2.549	2.307
$E_{surf}\{211\}$	2.989		3.351[h]	3.045	3.045	3.045	2.581	2.969	2.780
$E_{surf}\{111\}$	3.263		3.455[h]	3.299	3.299	3.299	3.088	3.254	2.948
$E_{surf}\{001\}$	2.893		3.924[h]	2.923	2.923	2.923	3.168	2.983	2.723
$a(fcc)$	4.10		4.00[i]	3.93	3.93	3.93	3.99	3.98	3.79
$\Delta E_{fcc-bcc}$	0.28		0.47[i]	0.15	0.15	0.15	0.05	0.09	0.37
$a(hcp)$	2.90			2.78	2.78	2.78	2.82	2.81	2.78
$\Delta E_{hcp-bcc}$	0.28			0.15	0.15	0.15	0.05	0.09	0.37
$a(sc)$	2.55		2.61[i]	2.58	2.60	2.60	2.75	2.67	2.63
ΔE_{sc-bcc}	2.04		1.25[i]	1.32	1.37	1.37	1.81	1.75	1.93
$a(diamond)$	6.25		5.87[j]	5.99	6.08	6.08	6.34	6.19	6.16
$\Delta E_{dia-bcc}$	3.45		2.33[j]	3.37	3.38	3.38	2.82	3.27	3.05
T_m	4580 ± 10	3695[k]			5200 ± 50[l]		3750[l]	4100 ± 50	

[a] Ref. [55].
[b] Ref. [58].
[c] Ref. [60].
[d] Ref. [73].
[e] Ref. [74].
[f] Ref. [59].
[g] Ref. [35].
[h] Ref. [29].
[i] Ref. [56].
[j] Ref. [57].
[k] Ref. [62].
[l] Ref. [63].

experimental measurements to more than 300 GPa, indicating that this potential can also reasonably describe the *P-V* relationships even at a non-equilibrium state. The equation of state obtained by the present potential also agrees well with the prediction of Rose's equation [54], as shown in Fig. 4(a).

In Fig. 5, the stacking fault energies for 1/2<111> {110} and 1/2<111> {112} shears, predicted by both DFT [29] and empirical potentials (FS, AT, JW, DN, WZ, MV2 and present work), are shown. For a {110} γ-surface, as shown in Fig. 5(a), the present potential prediction is close to the first-principles calculation, better than other potentials. For a {112} γ-surface, as shown in Fig. 5(b), all the empirical potentials show the similar symmetrical trend and the peak value predicted by the present potential is also closer to the DFT result [29].

Except the properties of above defects in W, the relative stability of 1/2<111> and <100> interstitial dislocation loops was also studied by using the present and other potentials (FS, AT, DN, WZ, MV2). In the present study, the hexagonal loops are built when the number of interstitials in such loop is less than 61, which have the lowest energy states. When the number of interstitials in a loop is more than 61, the hexagonal and circular loops show the similar states, which both have lower energy than the square loops. Thus, the circular loops are built for further studies. The formation energies of 1/2<111> and <100> loops as a function of the number of interstitials are calculated, which are fully relaxed with molecular statics method, and the results are shown in Fig. 6. With the present potential, the 1/2<111> loops are energetically favored for all sizes, while there is no significant difference predicted by FS and AT potentials. On the contrary, DN, WZ and MV2 potentials predict the reversed relative stability above a certain size, which is in contradiction with experimental observations [39–41]. Thus, in the case of radiation induced interstitial dislocation loops in W, the present potential will be more suitable for studying their properties and predicting loop formation under irradiation.
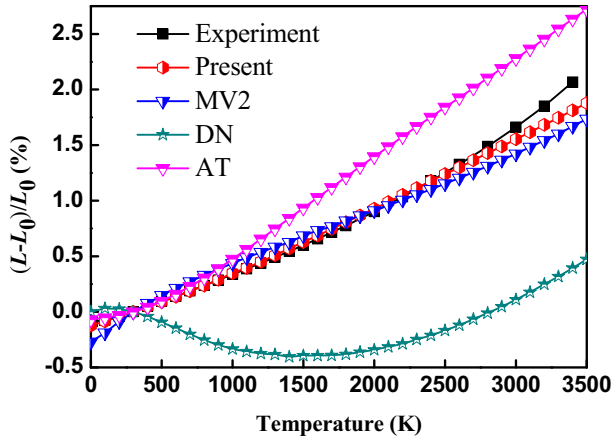
Fig. 2. Thermal expansion of W derived from different interatomic potentials (AT [32], DN [35], MV2 [37] and present work) in comparison with the experimental results [36].
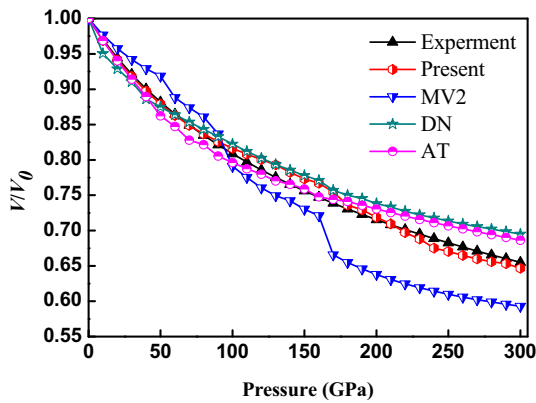

Fig. 3. Pressure-volume relation for W computed with different interatomic potentials (AT [32], DN [35], MV2 [37] and present work) in comparison with the experiment calculations [64].

Fig. 4. Comparison of equation of state calculated with the present potentials and results obtained with Rose's equation [54]. (a) and (b) show the above comparison of W and Re, respectively. In the figure, the solid curve is the result calculated from the present potential and the dashed curve is the result from the Rose equation [54].

Fig. 7 shows the relaxed core structure of a 1/2<111> screw dislocation in W, presented as a differential displacement map [65]. The degenerate core was predicted with the present W potential. In fact, the similar degenerate core structure has also been predicted by other empirical potentials (FS, AT, JW, DN, WZ) [29,37,38]. However, DFT predicts a compact core structure for a 1/2<111> screw dislocation [66,67], which indicates that the present W potential still needs improvement in describing this property.

3.2. Validation of the present Re potential

The properties of Re calculated using the present potential are also summarized in Table 3, along with available experimental data and the predictions of DFT and other EAM potentials [28] for comparison. The properties marked with a "*" are also those considered in the fitting process.

From Table 3, it is clear that the present Re potential reproduces the cohesive energy and lattice constants of the input fitting parameters, or the experiment values [55,68]. The elastic constants calculated also agree well with the experimental data [69], and the differences of the elastic constants between the present calculations and the experimental results are less than 5%.

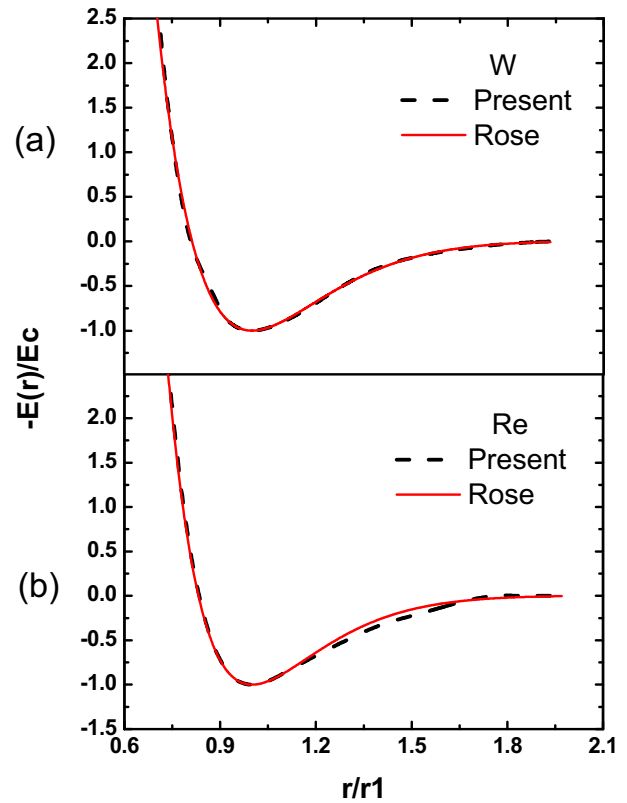The vacancy formation energy calculated with the present potential is 3.20 eV, close to the DFT result (3.12 eV) [70]. The surface energies of the basal and prism planes obtained with the present potential are 2.11 and 2.72 J/m^2, respectively, indicating that the basal plane is more stable than the prism plane, which is also the same as the DFT prediction, although the present surface energies are somewhat lower than the DFT results (2.58 against 2.92 J/m^2) [71].

The structural energy differences calculated with the present potential are also listed in Table 3, together with the values obtained from other calculations and DFT results [72]. The present potential reproduces well the energy order of those different structures, which is the same as the EAM potential [28], although the structural energy differences are smaller than the DFT values [72]. Fig. 8 shows the energy-volume relations for the lattice structures of bcc, fcc, hcp (real c/a) and hcp (ideal c/a). It is obvious that the fitted hcp lattice is the most stable state. The mechanical stability of the hcp lattice with respect to large homogeneous expansions and compressions has also been tested with the present potential by calculating the energies of the hcp crystal with different values of the atomic volume and c/a ratio. Fig. 9 shows the dependence of cohesive energy on c/a ratio at the different values of volume for Re. In a given range of the c/a ratios and atomic volumes, the hcp with the present a and c lattice constants is the most stable one. Except the above dependence, the relation between the energy and volume predicted with the present potential is also in fair agreement with the prediction by Rose's equation [54], as shown in Fig. 4(b).

The melting temperature for Re was also determined using the present potential with the solid-liquid coexistence method [61] by performing the MD simulations with a $14\sqrt{3}a_0 \times 24a_0 \times 30c_0$ simulation box containing 40,320 atoms. The melting temperature
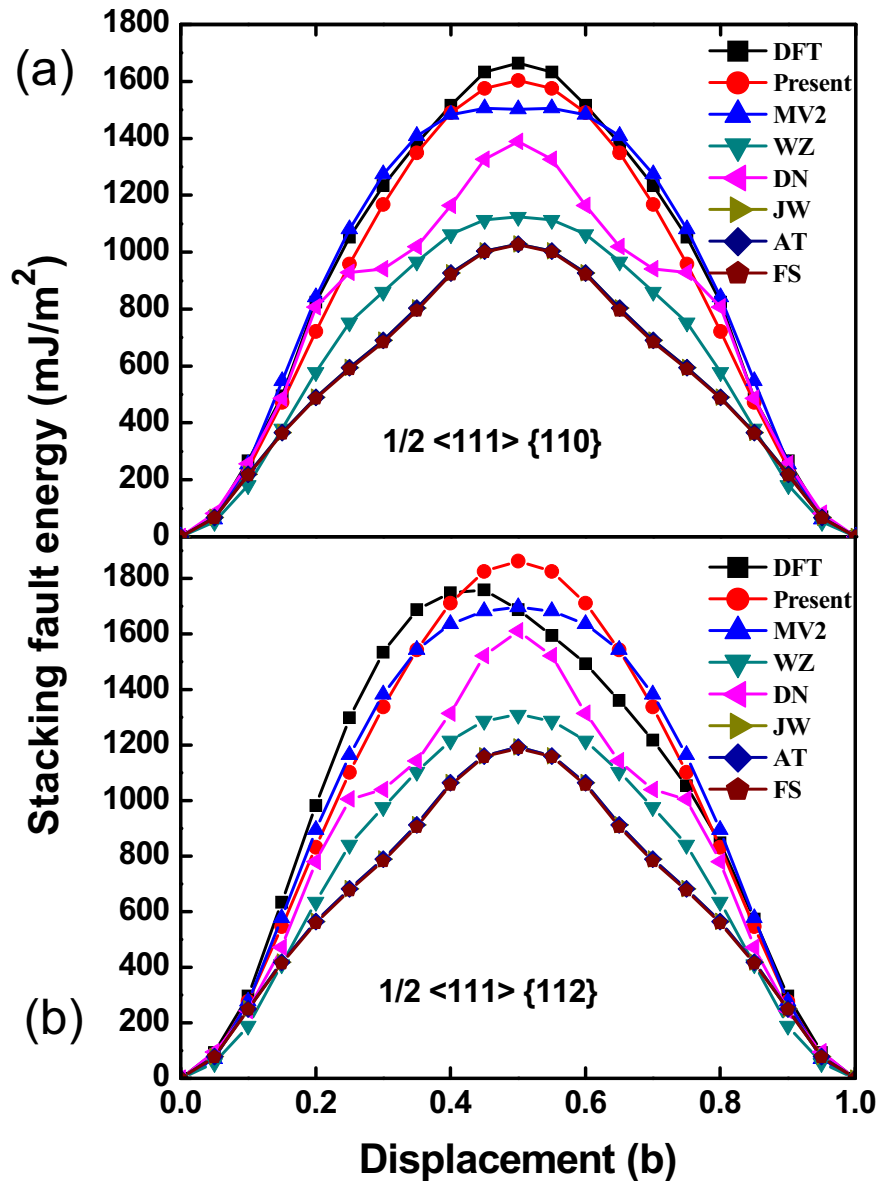
Fig. 5. Stacking fault energy (γ) of (a) {110} and (b) {112} surfaces calculated with different interatomic potentials and by DFT [29]. Potentials include FS [33], AT [32], JW [34], DN [35], WZ [38], MV2 [37] and present work.

is 3725 ± 10 K for Re, which is about 300 K higher than the experimental value of 3459 K [55]. For EAM potential [28], the melting temperature is 4836 K.

### 3.3. Validation of the present W-Re potential

As fitting the W-Re potential, the properties of some important irradiation defects for Re in bulk W calculated using the DFT method have been used as the inputs to determine the potential parameters. Those defect properties include the formation energy of a substitutional Re atom, the binding energy between a Re atom and a vacancy, the formation energy difference between a <111> Re-W mixed dumbbell and a <110> Re-W mixed dumbbell, the formation energy of a Re-Re dumbbell, the binding energy between a substitutional Re and an interstitial Re, and other properties (indicated by "*" in Table 4). The key behaviors of Re with different point defects in bcc W are summarized in Table 4, where the values calculated with the present potential,

EAM potential [28] and DFT [20,23,25,70] are presented.

From Table 4, it is clear that the calculated formation energy of a substitutional Re atom agrees well with the DFT value [23,25]. As for Re interstitial in the form of mixed dumbbell structures, the most energetically stable configuration is along the <111> direction with the formation energy of 9.04 eV, very close to the DFT calculations (9.12 eV [70], 9.17 eV [20]) and much better than the prediction of EAM potential with a value of 9.77 eV [28]. Furthermore, the present potential shows that the formation energy difference between the <111> mixed dumbbell and <110> mixed dumbbell is rather small (0.02 eV), agreement quit well with the DFT results (0.03 eV [20], 0.02 eV [70]). This formation energy difference is very important for the Re diffusing and clustering in W bulk. Clearly, the EAM potential strongly overestimated this energy (0.42 eV [28]).

We further investigate the migration of one Re-W mixed dumbbell in bulk W by MD simulations. The computational box contains 20 unit cells with X-, Y- and Z-axis along the [100], [010]
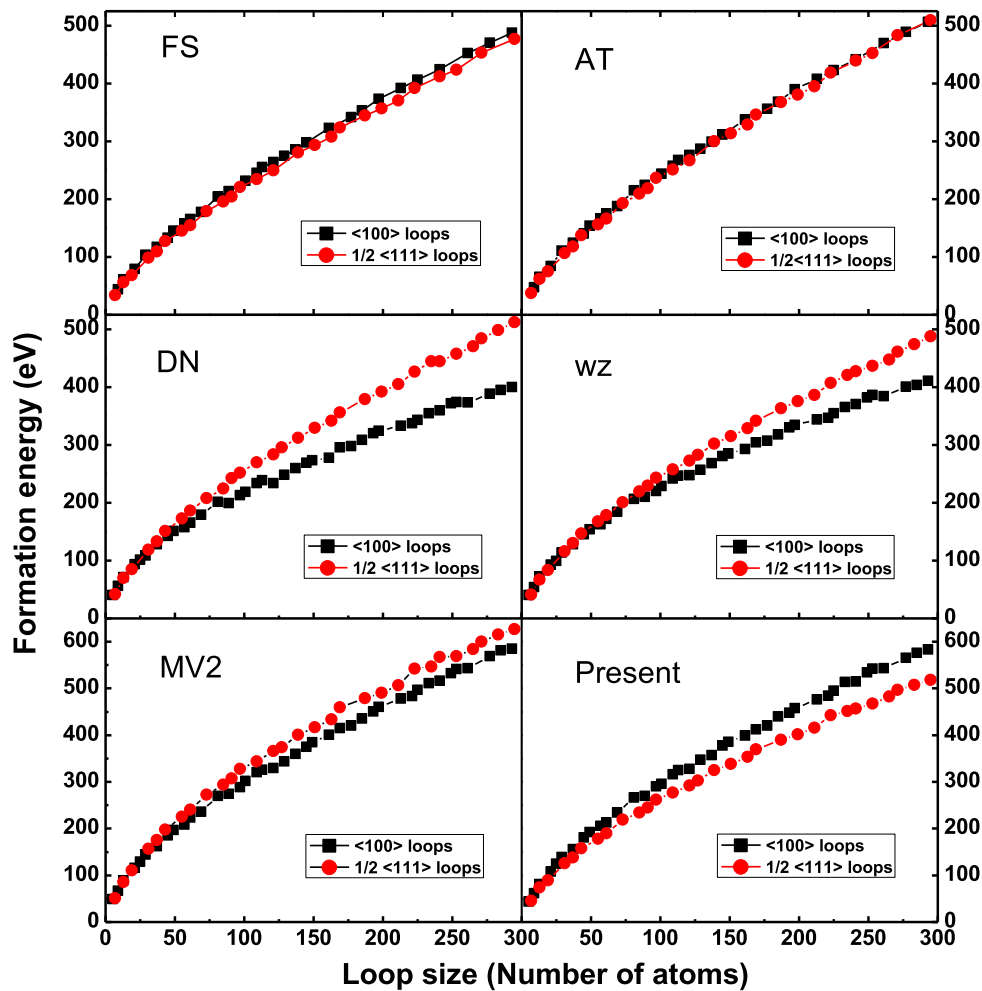
Fig. 6. Loop formation energy as a function of number of interstitials calculated with the different potentials (FS [33], AT [32], DN [35], WZ [38], MV2 [37] and present work). The results of 1/2<111> loops and <100> loops are shown with red and black squares, respectively. (For interpretation of the references to colour in this figure legend, the reader is referred to the Web version of this article.)

and [001] direction, respectively, which consists of 16,001 atoms in such a matrix by adding one Re-W mixed dumbbell defect. The evolution of the defect has been studied over the temperature range 300−800 K. For each temperature case, the total simulation time is up to 2.0 ns. The diffusion coefficient of the Re-W dumbbell has been calculated with mean square displacement (MSD) method and provided in Fig. 10. It is clear that the migration energy of Re-W dumbbell in bulk W is 0.15 eV, close to the DFT value of 0.11 eV [70]. Except the diffusion of Re through Re-W mixed dumbbell mechanism, we calculated the diffusion of a single Re or W through vacancy mechanism. From Tables 2 and 4, it is clear that the migration energy barrier of W and Re through vacancy-mediated way predicted by the present potential is 1.91 eV and 1.46 eV, respectively, which is slightly different from the results of DFT calculations (1.78 eV and 1.65 eV) [20,59]. The difference in migration energy barrier for Re-vacancy and W-vacancy is 0.13 eV from DFT calculation and 0.45 eV from the present potential. Although this larger difference will lead to an overestimation of Re diffusion compared to W through vacancy mechanism, it can be clearly found that the migration energy barrier through the vacancy-mediated way is much larger than that through the interstitial-mediated way, which suggests that interstitial-mediated migration could dominate the migration of Re in W under irradiation condition.

Fig. 11 shows the binding energy of a Re-vacancy (Re-Vac) pair as a function of the distance between the Re atom and vacancy. The binding energies between the Re and vacancy located at the first and second neighbor sites predicted by the present potential are 0.20 eV and 0.18 eV, respectively, which is close to the DFT results (0.24 eV and 0.21 eV) [25]; while the EAM potential [28] underestimates these values (with the both values of 0.06 eV). Thus, the present potential well reproduces the DFT calculations of the binding properties of Re with a vacancy in W.

The binding energies between a substitutional Re and an interstitial W are also calculated and listed in Table 4. Both DFT [20,70] and the present empirical potential predict that the <111> W-Re mixed dumbbell has the highest binding energy, while the <100> mixed dumbbell has a negative value. These results indicate that the <111> mixed dumbbells are preferred to form when the substitutional Re atoms are close to interstitial W atoms created by irradiation. This feature is well reproduced by the present potential although its value is slightly lower than that of the DFT predication [20,70]. The EAM potential [28] well reproduces the <111> W-Re mixed dumbbell, but the <110> mixed dumbbell is underestimated with about 0.4 eV lower than the DFT result [70].

The stability of Re-Re dumbbells in bcc bulk W has also been tested with the present potential. The <110> dumbbell is the most stable configuration predicted by this potential, which is same as
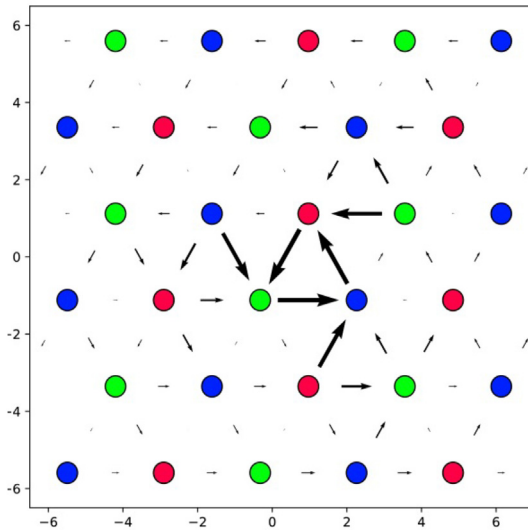
Fig. 7. Different displacement map of the 1/2<111> screw dislocation according to our present W potential. The atomic arrangement is shown in the projection perpendicular to the direction of the dislocation line, and circles represent atom positions in three successive (111) planes distinguished by shading. The arrows are drawn between pairs of neighboring atoms on the projections. The length of the arrows is proportional to the difference of the [1 1 1] displacements of the neighboring atoms, and normalized such that the longest arrow is equal to the separation of the atoms in the projection.

the results of DFT [70] and EAM potential [28] calculations, as listed in Table 4. Comparing with the result from EAM potential [28], the present potential gives a closer formation energy to the DFT result [70]. The binding energy between a substitutional Re and a mixed W-Re <111> dumbbell is also calculated. Although both the empirical potentials underestimate such binding energy, the present potential shows the prediction closer to the DFT results [70] than the EAM potential [28].

Table 3
Properties of pure Recalculated using the present potential, in comparison with the experimental values and calculations of the EAM potential or DFT method. Properties indicated by "*" were included in the fit. The following values are listed: the lattice parameter a and c (Å), the cohesive energy E_c (eV), the elastic constants C_{11}, C_{12}, C_{13}, C_{33} and C_{44} (GPa), the vacancy formation energy E_v^f (eV), the surface energy E_{Surf} (J/m^2), the structural energy difference ΔE (eV), and the melting point (K).

Property	Present	EXP./DFT	EAM [28]
a (hcp)*	2.760	2.760[a]	2.761
c (hcp)*	4.458	4.458[a]	4.456
E_c(hcp)*	8.03	8.03[b]	8.03
C_{11}^*	603	616[c]	611
C_{12}^*	285	273[c]	299
C_{13}^*	206	206[c]	234
C_{33}^*	682	683[c]	682
C_{44}^*	162	161[c]	159
E_v^{f*}	3.20	3.12[d]	3.49
E_{surf}(basal)	2.109	2.581[e]	2.249
E_{surf}(prism)	2.723	2.923[e]	2.979
a (fcc)	3.896	3.928[f]	3.900
$\Delta E_{fcc-hcp}$	0.02	0.06[f]	0.02
a (bcc)	3.085	3.125[f]	3.048
$\Delta E_{bcc-hcp}$	0.22	0.32[f]	0.13
T_m	3725 ± 10	3459[b]	4836

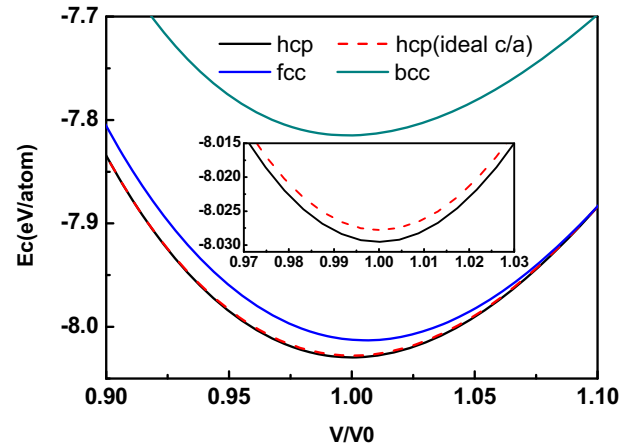[a] Experiment, Ref. [68].
[b] Experiment, Ref. [55].
[c] Experiment, Ref. [69].
[d] DFT, Ref. [70].
[e] DFT, Ref. [71].
[f] DFT, Ref. [72].

Fig. 8. The energy-volume relations for bcc, fcc, hcp (real c/a) and hcp (ideal c/a) structures calculated with the present potential.

The interactions between multiple Re atoms and vacancies have also been investigated with the present potential for that the Re-Vac cluster may act as an initial seed for the formation of solute precipitates. The total binding energies of Re$_n$ clusters and Re$_n$Vac clusters in bulk W are presented in Fig. 12(a) and Fig. 12(b), respectively. Based on DFT calculations [26], the total binding energies of Re$_n$ clusters in bulk W are negative (as shown in Fig. 12(a)), which indicates that the interactions between Re atoms are repulsive; however, obtained by the present W-Re potential, the total binding energies of Re$_n$ clusters in bulk W are positive, which indicates that the interactions between Re atoms are attractive. It can be found the total binding energies of Re$_n$Vac clusters are
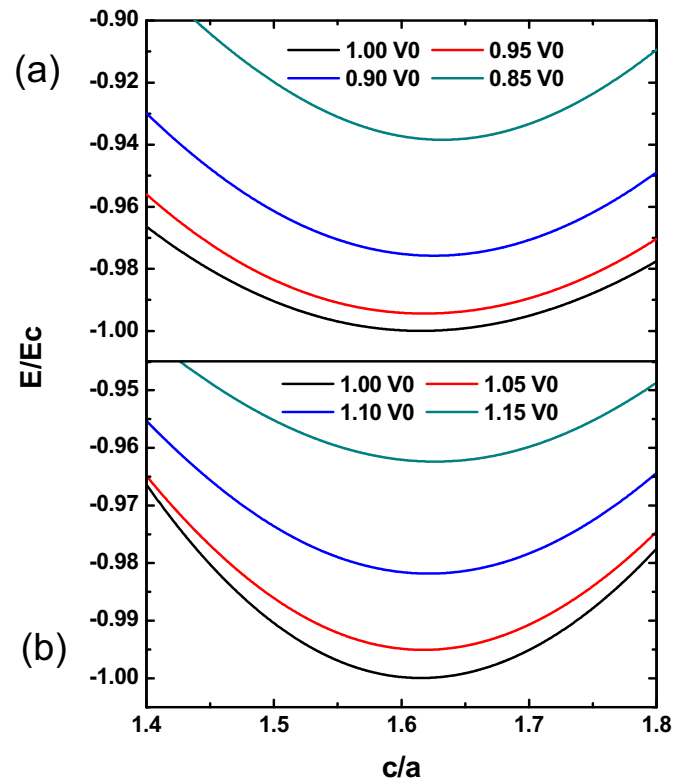
Fig. 9. Dependence of cohesive energy on c/a ratio at different values of the atomic volume of Re.
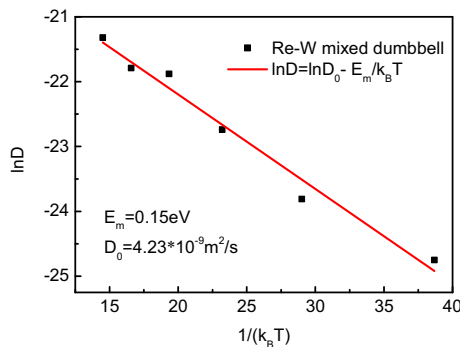
Table 4

Summary of the key behaviors of Re with point defects in bcc bulk W using the present potential, in comparison with the experimental values and calculations of the EAM potential or DFT method. Properties indicated by "*" were included in the fit. The following values are listed: the formation energy of a substitutional Re atom ($E_{sub}^f(Re)$), the binding energy of two substitutional Re atoms ($E_{sub}^b(Re - Re)$), the binding energy between Re atom and vacancy ($E^b(Re - Vac)$), the migration energy barrier of Re through vacancy-mediated way and interstitial-mediated way (E^m), the formation energy of Re-W mixed dumbbell ($E^f(Re - W)$), the formation energy difference between the <111> Re-W mixed dumbbell and the <110> Re-W mixed dumbbell ($\Delta E_{<110> - <111>}(Re - W)$), the binding energy between Re and SIAs ($E^b(Re - W)$), the formation energy of Re-Re dumbbell ($E^f(Re - Re)$), the binding energy between a substitutional Re and interstitial Re ($E^b(Re - Re)$). The units of the energy are all given in eV.

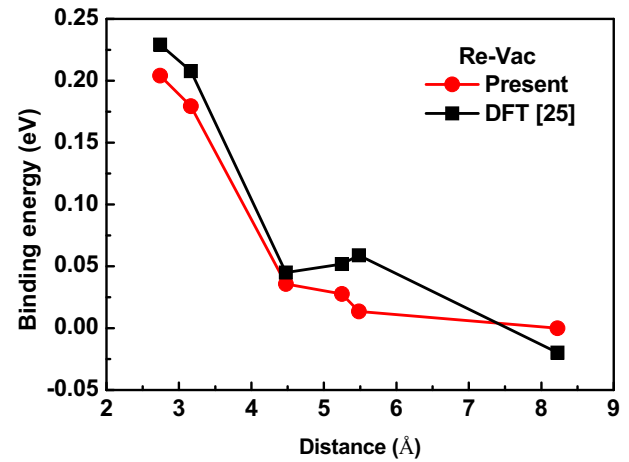| Property	Present	DFT	EAM [28]
$E_{sub}^f(Re)$*	0.17	0.17[a],0.19[b]	0.17
$E_{sub1nn}^b(Re - Re)$	0.13	−0.07[b],-029[c]	0.16
$E_{sub2nn}^b(Re - Re)$	−0.11	−0.02[b],-0.20[c]	−0.07
$E_{1nn}^b(Re - Vac)$*	0.20	0.22[d],0.24[b]	0.06
$E_{2nn}^b(Re - Vac)$*	0.18	0.22[d],0.21[b]	0.06
$E^m(Re - Vac)$	1.46	1.65[d]	1.81
$E^m(Re - W)$	0.15	0.11[e]	
$E_{<111>}^f(Re - W)$*	9.04	9.17[d],9.12[e]	9.77
$E_{<110>}^f(Re - W)$*	9.06	9.20[d],9.14[e]	10.19
$E_{<100>}^f(Re - W)$	9.72	10.20[d],11.03[e]	11.45
$\Delta E_{<110> - <111>}(Re - W)$*	0.02	0.03[d],0.02[e]	0.42
$E_{<111>}^b(W - Re)$*	0.60	0.79[d],0.78[e]	0.80
$E_{<110>}^b(W - Re)$	0.57	0.77[e]	0.38
$E_{<100>}^b(W - Re)$	−0.10	−1.17[e]	−0.88
$E_{<111>}^f(Re - Re)$	9.03	8.64[e]	9.90
$E_{<110>}^f(Re - Re)$*	8.91	8.19[e]	9.87
$E_{<100>}^f(Re - Re)$	10.43	10.41[e]	11.40
$E_{<111>}^b(Re - Re)$	0.17	0.50[e]	0.03
$E_{<110>}^b(Re - Re)$*	0.30	0.95[e]	0.07
$E_{<100>}^b(Re - Re)$	−1.22	−1.27[e]	−1.46

[a] Ref. [23].
[b] Ref. [25].
[c] Ref. [26].
[d] Ref. [20].
[e] Ref. [70].

Fig. 11. Binding energy of Re-Vac pair as a function of the distance between Re and vacancy.

Re$_n$Vac cluster is energetically preferred to be formed than the Re$_n$ cluster with the same Re atoms. Both DFT calculations [25,26] and our present calculations suggest that vacancy can contribute to the clustering of Re, that is, the vacancy can act as one of possible nucleation sites for Re impurities in bulk W.

Fig. 13 shows the binding energy of a Re atom to a Re$_{m-1}$Vac$_n$ cluster with the present potential, as compared to the DFT calculations [25]. The binding energies predicted by the present potential are positive and close to the DFT results [25], suggesting that Re atoms and vacancies prefer to aggregate in bulk W. Based on the difference between the binding energies of Vac-Vac, Re-Vac and Re-Re in bulk W, it is clear that when there are only vacancies and Re interstitials, the newly formed Re atoms would prefer to form Re$_2$ clusters and then ReVac cluster while the vacancy would prefer to form Vac$_2$ cluster and then ReVac cluster. However, it should be noted that once the interstitial W atoms exist, the W-Re mixed dumbbell is firstly formed and then the Re-Vac cluster.

4. Conclusions

In this paper, we have developed new interatomic potentials of W-W, Re-Re and W-Re for simulating the radiation damage in W-Re systems, which are based on the F-S formalism. The potentials have been fitted to an extensive database from experiments as well as first-principles DFT calculations. For W-W interaction, the potential well reproduced the formation and migration energies of simple defects. More importantly, the present W-W potential correctly predicts the relative stability of radiation induced dislocation loops with the Burgers vectors of 1/2<111> and <100> in W (the 1/2<111> loops are the most stable). For Re-Re interaction, the basic properties (lattice constants, cohesive energy, bulk modulus, elastic constants, vacancy formation energy) are good in agreement with the experimental results. For W-Re, the key point-defect properties of Re in W are close to DFT values, especially the binding and migration energies related to the clustering and precipitation of Re-rich defects in W. Thus, the potentials provide possible applications to describe the radiation damage in W and W-Re alloys, and are capable of simulating the defect evolutions in tungsten and tungsten rhenium alloy, providing a possibility for a detailed understanding of the precipitation mechanisms of Re in W under irradiation.

positive obtained by both the present W-Re potential and DFT calculations [26], and the binding energy increases with the increasing of the sizes of Re clusters. Therefore, the DFT results indicate that the clustering of Re atoms in defect-free W is nearly impossible, but Re atoms can aggregates around a vacancy when there exists a vacancy; whereas, the results obtained from the present potential indicate that the interactions between Re atoms are attractive in bulk W whether a vacancy exists or not, and the

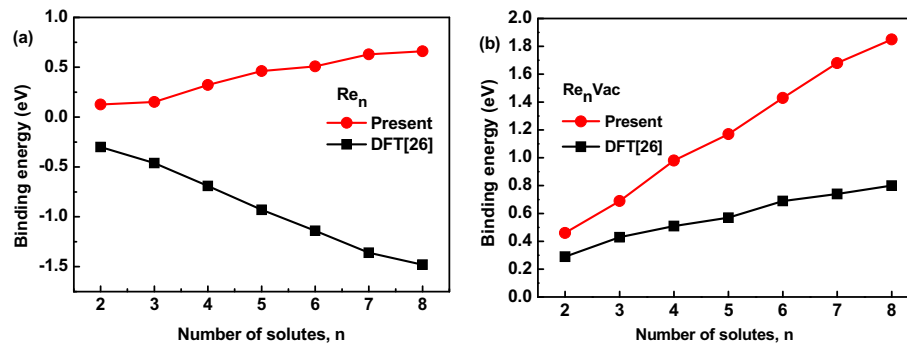**Fig. 10.** Diffusion coefficient for Re-W mixed dumbbell. The lines are linear Arrhenius fits.

Fig. 12. (a) Total binding energies of Re_n clusters as a function of the number of substitutional solute Re atoms in the system. **(b)** Total binding energies of Re_nVac clusters containing multiple substitutional solute Re atoms around a vacancy.
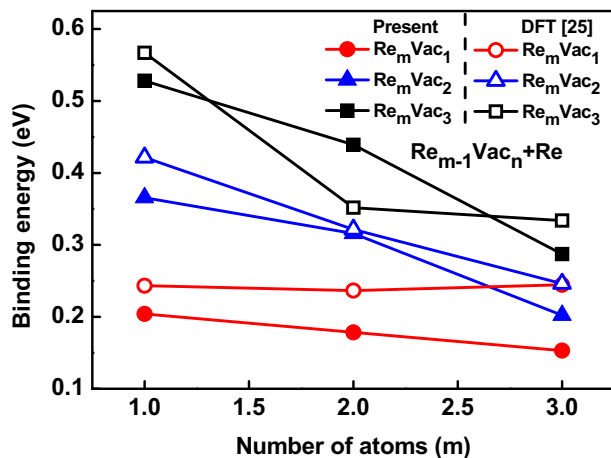

Fig. 13. Binding energy of Re to $Re_{m-1}Vac_n$ cluster as a function of the number of Re atoms in formed Re_mVac_n cluster.

Acknowledgements

References

[1] H. Bolt, V. Barabash, W. Krauss, et al., Materials for the plasma-facing components of fusion reactors, J. Nucl. Mater. 329–333 (2004) 66–73.
[2] R. Neu, V. Bobkov, R. Dux, et al., Final steps to an all tungsten divertor tokamak, J. Nucl. Mater. 363–365 (2007) 52–59.
[3] K. Wittlich, T. Hirai, J. Compan, et al., Damage structure in divertor armor materials exposed to multiple ITER relevant ELM loads, Fusion Eng. Des. 84 (2009) 1982–1986.
[4] M. Rieth, S.L. Dudarev, S.M. Gonzalez de Vicente, et al., Recent progress in research on tungsten materials for nuclear fusion applications in Europe, J. Nucl. Mater. 432 (2013) 482–500.
[5] E. Lassner, W.D. Schubert, Tungsten: Properties, Chemistry, Technology of the Element, Alloys, and Chemical Compounds, Springer, Berlin, 2011.
[6] G. Federici, C.H. Skinner, J.N. Brooks, et al., Plasma-material interactions in current tokamaks and their implications for next step fusion reactors, Nucl. Fusion 41 (2001) 1967.
[7] G.A. Cottrell, R. Pampin, N.P. Taylor, Transmutation and phase stability of tungsten armor in fusion power plants, Fusion Sci. Technol. 50 (2006) 89–98.
[8] M.R. Gilbert, J.-Ch Sublet, Neutron-induced transmutation effects in W and W-alloys in a fusion environment, Nucl. Fusion 51 (2011), 043005.
[9] M. Ekman, K. Persson, G. Grimvall, Phase diagram and lattice instability in tungsten-rhenium alloys, J. Nucl. Mater. 278 (2000) 273–276.
[10] B. Ralph, D.G. Brandon, A field ion microscope study of some tungsten-rhenium alloys, Philos. Mag. A 8 (1963) 919–934.
[11] Y. Nemoto, A. Hasegawa, M. Satou, et al., Microstructural development of neutron irradiated W-Re alloys, J. Nucl. Mater. 283–287 (2000) 1144–1147.
[12] T. Tanno, A. Hasegawa, J.C. He, et al., Effects of transmutation elements on the microstructural evolution and electrical resistivity of neutron-irradiated tungsten, J. Nucl. Mater. 386–388 (2009) 218–221.
[13] T. Tanno, M. Fukuda, S. Nogami, et al., Microstructure development in neutron irradiated tungsten alloys, Mater. Trans. 52 (2011) 1447–1451.
[14] A. Hasegawa, M. Fukuda, T. Tanno, et al., Neutron irradiation behavior of tungsten, Mater. Trans. 54 (2013) 466–471.
[15] M. Fukuda, K. Yabuuchi, S. Nogami, et al., Microstructural development of tungsten and tungsten-rhenium alloys due to neutron irradiation in HFIR, J. Nucl. Mater. 455 (2014) 460–463.
[16] A. Xu, D.E. Armstrong, C. Beck, et al., Ion-irradiation induced clustering in W-Re-Ta, W-Re and W-Ta alloys: an atom probe tomography and nano-indentation study, Acta Mater. 124 (2017) 71–78.
[17] A. Xu, C. Beck, D.E. Armstrong, et al., Ion-irradiation-induced clustering in W-Re and W-Re-Os alloys: a comparative study using atom probe tomography and nanoindentation measurements, Acta Mater. 87 (2015) 121–127.
[18] X.-S. Kong, X. Wu, Y.-W. You, et al., First-principles calculations of transition metal-solute interactions with point defects in tungsten, Acta Mater. 66 (2014) 172–183.
[19] W.-L. Yan, H.-B. Zhou, S. Jin, et al., Dissolution energetics and its strain dependence of transition metal alloying elements in tungsten, J. Nucl. Mater. 456 (2015) 260–265.
[20] T. Suzudo, M. Yamaguchi, A. Hasegawa, Stability and mobility of rhenium and osmium in tungsten: first principles study, Model. Simulat. Mater. Sci. Eng. 22 (2014) 075006.
[21] T. Suzudo, M. Yamaguchi, A. Hasegawa, Migration of rhenium and osmium interstitials in tungsten, J. Nucl. Mater. 467 (2015) 418–423.
[22] L. Gharaee, J. Marian, P. Erhart, The role of interstitial binding in radiation induced segregation in W-Re alloys, J. Appl. Phys. 120 (2016), 025901.
[23] L. Gharaee, P. Erhart, A first-principles investigation of interstitial defects in dilute tungsten alloys, J. Nucl. Mater. 467 (2015) 448–456.
[24] W. Setyawan, G. Nandipati, R. Kurtz, Ab initio study of interstitial cluster interaction with Re, Os, and Ta in W, J. Nucl. Mater. 484 (2017) 30–41.
[25] Y.-H. Li, H.-B. Zhou, S. Jin, et al., Behaviors of transmutation elements Re and Os and their effects on energetics and clustering of vacancy and self-interstitial atoms in W, Nucl. Fusion 57 (2017), 046006.
[26] Y.-W. You, X.-S. Kong, X. Wu, et al., Clustering of transmutation elements tantalum, rhenium and osmium in tungsten under a fusion environment, Nucl. Fusion 57 (2017), 086006.
[27] J.S. Wróbel, D. Nguyen-Manh, S.L. Dudarev, et al., A first-principles model for anomalous segregation in dilute ternary tungsten-rhenium-vacancy alloys, J. Phys. Condens. Matter 29 (2017), 145403.
[28] G. Bonny, A. Bakaev, D. Terentyev, et al., Interatomic potential to study plastic deformation in tungsten-rhenium alloys, J. Appl. Phys. 121 (2017), 165107.
[29] G. Bonny, D. Terentyev, A. Bakaev, et al., Many-body central force potentials for tungsten, Model. Simulat. Mater. Sci. Eng. 22 (2014), 053001.
[30] R.C. Ehemann, J.W. Nicklas, H. Park, et al., Ab initio based empirical potential applied to tungsten at high pressure, Phys. Rev. B 95 (2017), 184101.
[31] W.J. Szlachta, A.P. Bartók, G. Csányi, Accuracy and transferability of Gaussian approximation potential models for tungsten, Phys. Rev. B 90 (2014), 104108.
[32] G.J. Ackland, R. Thetford, An improved N-body semi-empirical model for body-centred cubic transition metals, Philos. Mag. A 56 (1987) 15–30.
[33] M.W. Finnis, J.E. Sinclair, A simple empirical N-body potential for transition metals, Philos. Mag. A 50 (1984) 45–55.
[34] N. Juslin, B.D. Wirth, Interatomic potentials for simulation of He bubble formation in W, J. Nucl. Mater. 432 (2013) 61–66.
[35] P.M. Derlet, D. Nguyen-Manh, S.L. Dudarev, Multiscale modeling of crowdion and vacancy defects in body-centered-cubic transition metals, Phys. Rev. B 76 (2007), 054107.
[36] G.K. White, M.L. Minges, Thermophysical properties of some key solids: an update, Int. J. Thermophys. 18 (1997) 1269–1327.

[37] M.-C. Marinica, L. Ventelon, M.R. Gilbert, et al., Interatomic potentials for modelling radiation defects and dislocations in tungsten, J. Phys. Condens. Matter 25 (2013), 395502.

[38] J. Wang, Y.L. Zhou, M. Li, et al., A modified W-W interatomic potential based on ab initio calculations, Model. Simulat. Mater. Sci. Eng. 22 (2014), 015004.

[39] X. Yi, M.L. Jenkins, K. Hattar, et al., Characterisation of radiation damage in W and W-based alloys from 2MeV self-ion near-bulk implantations, Acta Mater. 92 (2015) 163—177.

[40] X. Yi, M.L. Jenkins, M.A. Kirk, et al., In-situ TEM studies of 150 keV W+ ion irradiated W and W-alloys: damage production and microstructural evolution, Acta Mater. 112 (2016) 105—120.

[41] F. Ferroni, X. Yi, K. Arakawa, et al., High temperature annealing of ion irradiated tungsten, Acta Mater. 90 (2015) 380—393.

[42] M.R. Gilbert, S.L. Dudarev, M.-C. Marinica, et al., The Anomalous Stability of Mesoscale <100>Prismatic Dislocation Loops in Irradiated Tungsten: Experiment and Simulation, MRS Fall Meeting, Boston, 2012.

[43] M.I. Baskes, R.A. Johnson, Modified embedded atom potentials for HCP metals, Model. Simulat. Mater. Sci. Eng. 2 (1994) 147—163.

[44] W. Hu, B. Zhang, B. Huang, et al., Analytic modified embedded atom potentials for HCP metals, J. Phys. Condens. Matter 13 (2001) 1193—1213.

[45] R.A. Johnson, D.J. Oh, Analytic embedded atom method model for bcc metals, J. Mater. Res. 4 (1989) 1195—1201.

[46] G. Bonny, R.C. Pasianot, Gauge transformations to combine multi-component many-body interatomic potentials, Phil. Mag. Lett. 90 (2010) 559—563.

[47] X. Gan, S. Xiao, H. Deng, et al., Atomistic simulations of the Fe (001)-Li solid-liquid interface, Fusion Eng. Des. 89 (2014) 2894—2901.

[48] Y. Wu, W. Hu, S. Han, Theoretical calculation of thermodynamic data for gold-rare earth alloys with the embedded-atom method, J. Alloy. Comp. 420 (2006) 83—93.

[49] H. Deng, W. Hu, X. Shu, et al., Atomistic simulation of the segregation profiles in Mo-Re random alloys, Surf. Sci. 543 (2003) 95—102.

[50] J.P. Biersack, J.F. Ziegler, Refined universal potentials in atomic collisions, Nucl. Instrum. Meth. Phys. Res. 194 (1982) 93—100.

[51] F. Gao, H. Deng, H.L. Heinisch, et al., A new Fe-He interatomic potential based on ab initio calculations in α-Fe, J. Nucl. Mater. 418 (2011) 115—120.

[52] S. Kirkpatrick, C.D. Gelatt, M.P. Vecchi, Optimization by simulated annealing, Science 220 (1983) 671—680.

[53] M.F. Møller, A scaled conjugate gradient algorithm for fast supervised learning, Neural Network. 6 (1993) 525—533.

[54] J.H. Rose, J.R. Smith, F. Guinea, et al., Universal features of the equation of state of metals, Phys. Rev. B 29 (1984) 2963.

[55] C. Kittel, Introduction to Solid State Physics, eighth ed., Wiley, New York, 2005.

[56] M. Mrovec, R. Gröger, A.G. Bailey, et al., Bond-order potential for simulations of extended defects in tungsten, Phys. Rev. B 75 (2007), 104119.

[57] N. Juslin, P. Erhart, P. Träskelin, et al., Analytical interatomic potential for modeling nonequilibrium processes in the W-C-H system, J. Appl. Phys. 98 (2005), 123520.

[58] G. Simmons, H. Wang, Single Crystal Elastic Constants and Calculated Aggregate Properties: a Handbook, second ed., The MIT Press, Cambridge, MA, 1971.

[59] D. Nguyen-Manh, A.P. Horsfield, S.L. Dudarev, Self-interstitial atom defects in bcc transition metals: group-specific trends, Phys. Rev. B 73 (2006), 020101.

[60] K.D. Rasch, R.W. Siegel, H. Schultz, Quenching and recovery investigations of vacancies in tungsten, Philos. Mag. A 41 (1980) 91—117.

[61] J.R. Morris, C.Z. Wang, K.M. Ho, et al., Melting line of aluminum from simulations of coexisting phases, Phys. Rev. B 49 (1994) 3109.

[62] CRC Handbook of Chemistry and Physics, eighty-fifth ed., CRC, Boca, Raton, 2004.

[63] J. Fikar, R. Schäublin, Molecular dynamics simulation of radiation damage in bcc tungsten, J. Nucl. Mater. 386 (2009) 97—101.

[64] R.S. Hixson, J.N. Fritz, Shock compression of tungsten and molybdenum, J. Appl. Phys. 71 (1992) 1721—1728.

[65] V. Vitek, R.C. Perrin, D.K. Bowen, The core structure of ½ (111) screw dislocations in bcc crystals, Philos. Mag. A 21 (1970) 1049—1073.

[66] L. Romaner, C. Ambrosch-Draxl, R. Pippan, Effect of rhenium on the dislocation core structure in tungsten, Phys. Rev. Lett. 104 (2010), 195503.

[67] H. Li, S. Wurster, C. Motz, et al., Dislocation-core symmetry and slip planes in tungsten alloys: ab initio calculations and microcantilever bending experiments, Acta Mater. 60 (2012) 748—758.

[68] C.S. Barrett, T.B. Massalski, Structure of Metals, McGraw-Hill, New York, 1966.

[69] E.A. Brandes (Ed.), Smithells Metals Reference Book, Butterworths, London, 1983.

[70] Y.-H. Li, H.-B. Zhou, H.Q. Deng, et al., Towards understanding the mechanism of rhenium and osmium precipitation in tungsten and its implication for tungsten-based alloys, J. Nucl. Mater. (2018) in revision.

[71] D.-P. Ji, Q. Zhu, S.-Q. Wang, Detailed first-principles studies on surface energy and work function of hexagonal metals, Surf. Sci. 651 (2016) 137—146.

[72] Y. Wang, S. Curtarolo, C. Jiang, et al., Ab initio lattice stability in comparison with CALPHAD lattice stability, Calphad 28 (2004) 79—90.

[73] K. Heinola, T. Ahlgren, Diffusion of hydrogen in bcc tungsten studied with first principle calculations, J. Appl. Phys. 107 (2010), 113531.

[74] M. Muzyk, D. Nguyen-Manh, K.J. Kurzydłowski, et al., Phase stability, point defects, and elastic properties of W-V and W-Ta alloys, Phys. Rev. B 84 (2011), 104115.